Evaluating Seismic Beamforming Capabilities of Distributed Acoustic Sensing Arrays

Martijn P. A. van den Ende[1] and Jean-Paul Ampuero[1]

[1]Université Côte d'Azur, IRD, CNRS, Observatoire de la Côte d'Azur, Géoazur, France

Correspondence: M. van den Ende (martijn.vandenende@geoazur.unice.fr)

Abstract. The versatility and cost-efficiency of fibre-optic Distributed Acoustic Sensing (DAS) technologies facilitate geophysical monitoring in environments that were previously inaccessible for instrumentation. Moreover, the spatio-temporal data density permitted by DAS naturally appeals to seismic array processing techniques, such as beamforming for source location. However, the measurement principle of DAS is inherently different from that of conventional seismometers, providing measurements of ground strain rather than ground motion, and so the suitability of traditional seismological methods requires in-depth evaluation. In this study, we evaluate the performance of a DAS array in the task of seismic beamforming, in comparison with a co-located nodal seismometer array. We find that, even though the nodal array achieves excellent performance in localising a regional M_L 4.3 earthquake, the DAS array exhibits poor waveform coherence and consequently produces inadequate beamforming results that are dominated by the signatures of shallow scattered waves. We demonstrate that this behaviour is likely inherent to the DAS measurement principle, and so new strategies need to be adopted to tailor array processing techniques to this emerging measurement technology.

1   Introduction

Dense seismometer arrays play a central role in understanding various geological phenomena, including earthquake rupture behaviour (Kiser and Ishii, 2017; Meng et al., 2011), micro-seismicity (Inbal et al., 2016), fault zone structure (Zigone et al., 2019), and deep crustal and mantle geology (Jiang et al., 2018; Lin et al., 2013). Moreover, seismic arrays also serve civil protection purposes through monitoring nuclear test ban treaty violations (Ringdal and Husebye, 1982), monitoring volcano deformation and activity (Inza et al., 2011; Nakamichi et al., 2013), and potentially issuing earthquake early warnings (Meng et al., 2014). While the benefits of seismic arrays are evident, the deployment and maintenance of these arrays is (logistically) costly, and consequently they are often deployed as part of temporary campaigns.

The recent emergence of fibre-optic Distributed Acoustic Sensing (DAS; Hartog, 2017; Zhan, 2020) has opened up a plethora of possibilities and applications in seismic- and transient deformation monitoring. Fibre-optic cables are relatively inexpensive, require little to no maintenance, and can be deployed in environments that were previously impractical for or inaccessible to traditional seismometers, such as urban environments (Dou et al., 2017; Fang et al., 2020), glaciers and permafrost regions (Ajo-Franklin et al., 2017; Walter et al., 2020), deep boreholes (Cole et al., 2018; Lellouch et al., 2019), and in lakes and submarine environments (Lindsey et al., 2019; Sladen et al., 2019) – see also Zhan (2020) for a concise review of applications

in geosciences. DAS thus has an enormous potential to complement or replace nodal seismometer arrays. However, the measurement principles of DAS are inherently different from those of conventional seismometers (Zhan, 2020), which presents new challenges in interpreting DAS data. Traditional array processing techniques, such as seismic beamforming, need to be re-evaluated for the application to DAS data.

30   Even though several studies already reported first results on applying seismic beamforming to linear and L-shaped DAS arrays (Fang et al., 2020; Lindsey et al., 2019), the potential of DAS in beamforming requires further exploration. In this study, we directly compare beamforming results of data from a nodal seismometer array and from a co-located optical fibre cable at the Brady Hot Springs geothermal site, Nevada, USA (Feigl and the PoroTomo Team, 2018). Specifically, we analyse the recordings of the March 2016 M_L 4.3 Hawthorne earthquake, which occurred $150\,\mathrm{km}$ south of the Brady Hot Springs

35   site and was well captured by both the nodal and DAS arrays. The comparison suggests that the beamforming of the DAS-recorded waveforms is severely hampered by shallow seismic scattering and by spatial variations in phase velocities, to which DAS measurements are highly sensitive. This is consistent with previous theoretical findings that ground motion gradients (or strain) are more severely affected by small-scale heterogeneities than ground motions themselves. We conclude by putting these observations in a broader context of beamforming capabilities of DAS arrays of larger aperture, and their application in

40   seismic source monitoring and earthquake early warning.

2   Methods

2.1   The PoroTomo experiment

The Poroelastic Tomography (PoroTomo) project is a hydrogeological experiment conducted in March 2016 (phase II) at a geothermal site near Brady Hot Springs, Nevada, USA (Feigl and the PoroTomo Team, 2018) – see Fig. 1. For the purpose of

45   high-resolution monitoring of changes in rock-mechanical properties during operation of the enhanced geothermal system, an array of 238 Fairfield Nodal ZLand 3C seismometers was deployed over an area spanning 1500 by $500\,\mathrm{m}$, as well as several fibre-optic cables for Distributed Acoustic Sensing and Distributed Temperature Sensing. These fibre-optic cables were laid-out horizontally in a trench of $8700\,\mathrm{m}$ in total length and $0.5\,\mathrm{m}$ in depth, and vertically in a borehole down to $400\,\mathrm{m}$. The geothermal reservoir of Tertiary volcanic rocks is overlain by a thick alluvium of several hundreds of metres in thickness (Jolie

50   et al., 2015). The near-surface velocity structure of the site has been inferred from the analysis of high-frequency vibroseis sweeps and from Noise Correlation Functions (Feigl and the PoroTomo Team, 2018), showing strong variations over distances of tens of metres.

During the experiment, on 21 March 2016 at 07:37:10 UTC, an M_L 4.3 strike-slip earthquake occurred $150\,\mathrm{km}$ SSE of the geothermal site. The ground motion data of this event recorded by both the nodal and DAS arrays are available at the

55   National Geothermal Data Repository (Feigl, 2016a, b). For convenience, we downsample the nodal and DAS data to $100\,\mathrm{Hz}$, which is largely sufficient for the frequency bands selected in our analysis (up to $5\,\mathrm{Hz}$). An in-depth analysis of the ground motions in terms of frequency content, spatial variability of signal-to-noise ratios, and the comparison between DAS and nodal seismometers was performed by Wang et al. (2018). These authors also performed a preliminary beamforming analysis using
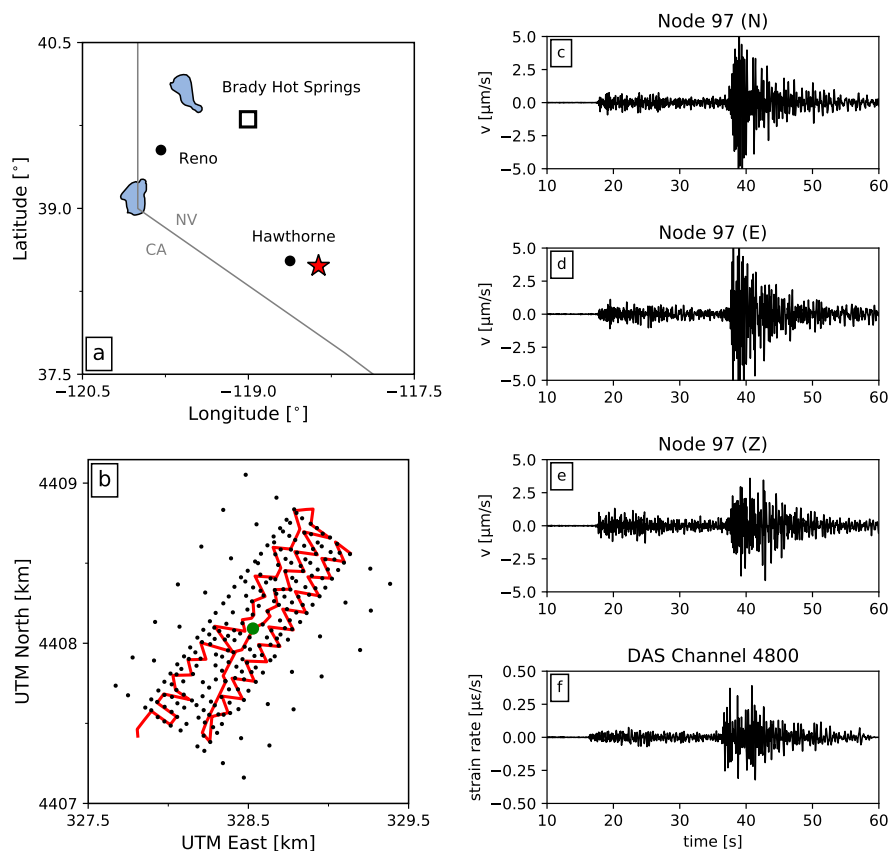
Figure 1. a) Location of the Brady Hot Springs natural laboratory and the March 2016 M_L 4.3 Hawthorne earthquake epicentre; b) Layout of the PoroTomo nodal seismometer array (black dots) and the fibre-optic cable (red line); c-e) Ground motions recorded on the N/E/Z-components of nodal seismometer #97, which is marked in panel b by a green dot; f) Strain rates recorded by a channel co-located with nodal seismometer #97. All waveforms are filtered in a 0.5-10 Hz pass band.

the data from the nodal seismometer array, but did not attempt to make a comparison with DAS data. In the present study, we
60 retrieve and interpret the same data set as was analysed by Wang et al. (2018), and so we build upon the conclusions drawn
from this previous study.

2.2 MUSIC beamforming

Seismic beamforming is a commonly employed array processing technique for estimating the direction-of-arrival (azimuth)
and slowness of the seismic waves arriving at a seismic array (Capon et al., 1967; Hutchison and Ghosh, 2017; Krüger et al.,
65 1993). It is assumed in most beamforming applications that the signal recorded at the k-th station in the array can be represented
by a superposition of N plane waves, each carrying a signal s and impinging on the array at an angle θ. We consider arrays

deployed at the surface, thus θ is the azimuth of propagation of the incident wave. Throughout the study we assume a single source ($N = 1$), so that the frequency-domain representation of the recorded signal can be written as:

$$x_k(\omega) = a_k(\omega, S, \theta)s(\omega) + e_k(\omega) \tag{1}$$

70   where e_k is the noise recorded at the k-th station, and $a_k = e^{i\omega\tau_k}$ is the steering vector that dictates the phase shift (time delay) of the signals at each station, relative to the centre of the array. The theoretical time delay $\tau_k = -S\left(\Delta x_k \sin\theta + \Delta y_k \cos\theta\right)$ is computed over a grid of candidate apparent slowness values S and azimuths θ, with a given station location $(\Delta x_k, \Delta y_k)$ relative to the centre of the array. In traditional delay-and-sum beamforming, the likelihood of each candidate in the grid of S and θ is estimated as the projection of the steering vector a onto the covariance matrix C^2, defined as:

75   $$C_{ij}^2 = \frac{x_i \bar{x}_j}{\sqrt{|x_i|^2 |x_j|^2}} \tag{2}$$

where $\bar{x}$ denotes the complex conjugate of x. Here, the spectra and cross-spectra involved in the equation above are estimated by the multi-taper method (Thomson, 1982), following Meng et al. (2011). Note that the covariance matrix is complex, and that it is scaled by the norms of the waveforms x such that $0 \le |C^2| \le 1$. Consequently, the magnitude of C^2 is not affected by amplitude differences between x_i and x_j, e.g. due to spatial variations in coupling or fibre orientation, which could be

80   represented as a station-specific factor $\alpha_k(\omega)$ multiplying the first term of the right-hand-side of Eq. (1). However, local effects leading to spatial variability of waveform shape are not compensated by this normalization.

MUltiple SIgnal Classification (MUSIC) is an extension of classical beamforming approaches that acknowledges sparsity in the number of signals arriving at the array, resulting in higher-resolution estimates of the back-azimuth and slowness of the seismic waves (Goldstein and Archuleta, 1987; Meng et al., 2011; Schmidt, 1986). Instead of projecting the steering vectors

85   onto the full covariance matrix, a pseudo-power of the signal is estimated as the reciprocal of the projection of the steering vectors onto the noise-space of the covariance matrix, which is found through an eigenvalue decomposition of C^2. For a detailed exposition of MUSIC, the reader is referred to Schmidt (1986).

3   Results

3.1   Signal characteristics and coherence

90   Before attempting to perform beamforming on the array data, we first consider the spectral characteristics of the recorded signals – see Fig. 2a and b. The velocity spectra of the three components of the wavefield recorded by the nodal array are first converted into acceleration spectra, which are proportional to the DAS strain rate spectra under the assumption of a single plane wave, with the phase velocity as the proportionality constant. An apparent phase velocity of $0.2\,\mathrm{km\,s^{-1}}$ for both the P- and S-phases gives a good comparison between the nodal spectra and the DAS spectra, which suggests that a common type of

95   wave (e.g. scattered surface waves) dominates the spectra of these time windows. For reference, the median power of the noise recorded by the nodal array prior to the P-wave arrivals is indicated by a grey band in Fig. 2. The durations of the noise, P-,
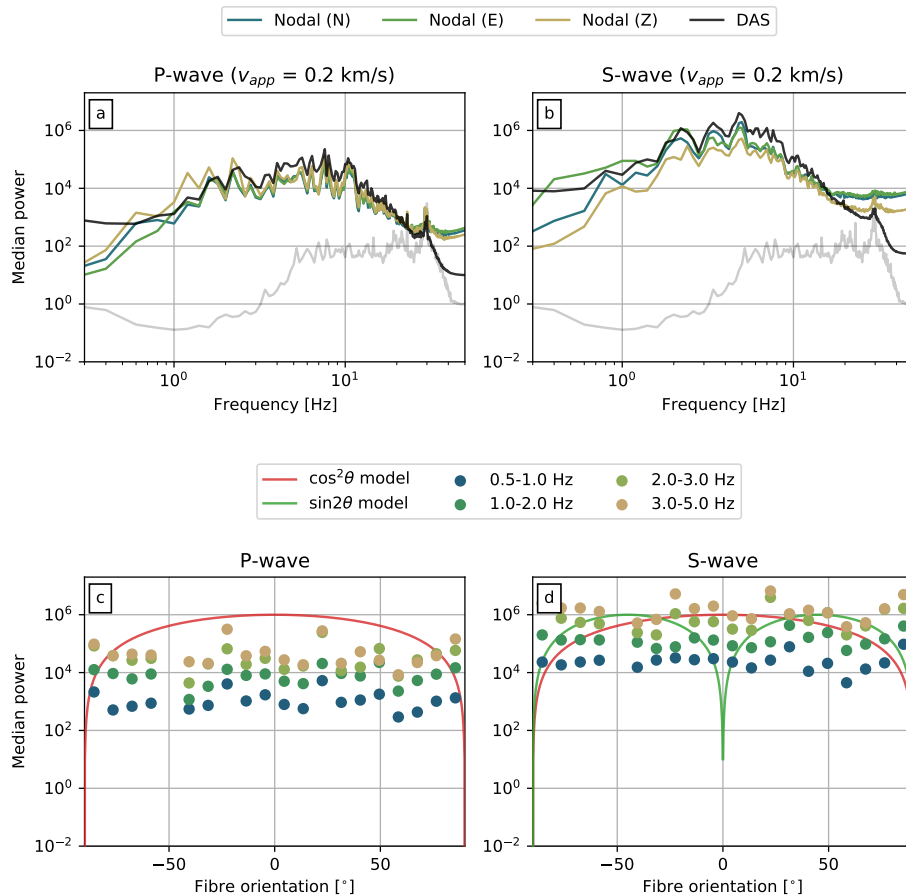
Figure 2. a-b) Median power spectral densities of the nodal and DAS arrays for the P-wave and S-wave. The nodal seismometer recordings are converted into acceleration spectra, which are proportional to the DAS strain rate spectra. The proportionality constant (the apparent phase velocity) is taken as $0.2 \ \mathrm{km \ s^{-1}}$. The noise floor is shown as a grey band; c-d) Mean power in selected frequency bins as a function of the fibre-optic cable orientation with respect to the back-azimuth of the seismic source. The theoretical sensitivities (Martin et al., 2018) are included for reference.

and S-wave windows over which the spectral power was computed are all taken to be $5 \ \mathrm{s}$, which is long enough to include low frequency information.

100   Owing to the nature of the measurement principle of DAS (i.e. measuring strains rather than particle motions), the directional sensitivity of the fibre to P- and S-waves is different from nodal seismometers (Kuvshinov, 2016; Zhan, 2020). For a gauge length that is much smaller than the seismic wavelength, the DAS strain rate is proportional to $\cos^2 \theta$ for a P-wave or SV-wave, and $\sin 2\theta$ for an SH-wave, assuming a plane wave with incidence angle θ relative to the fibre (Martin et al., 2018). These theoretical sensitivities are plotted for reference in Fig. 2c and d, alongside the mean power measured within selected fibre
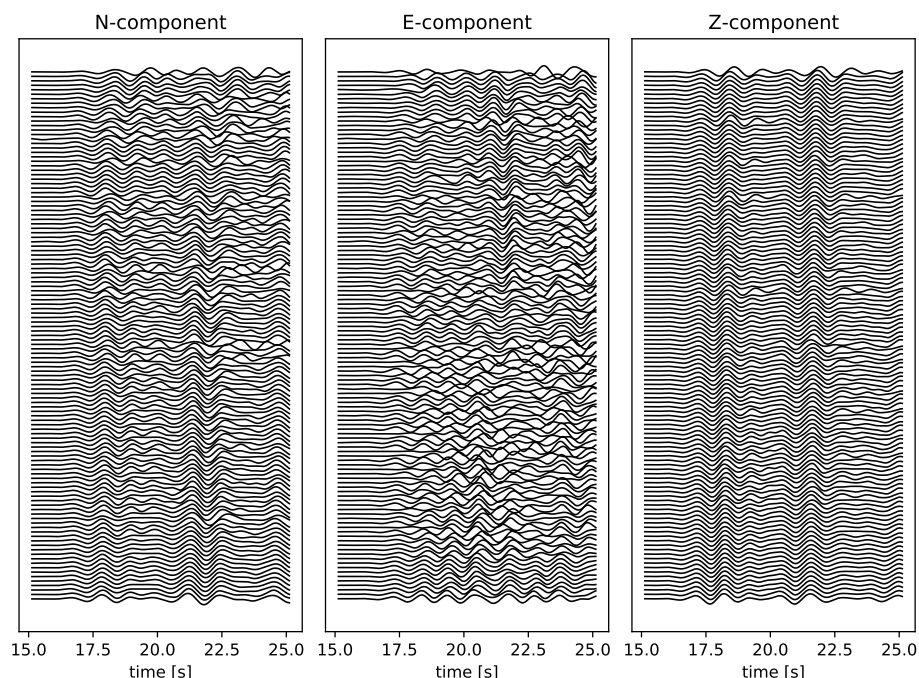
Figure 3. P-waveforms recorded by the nodal array, ordered by distance from the earthquake epicentre, band-pass filtered in the 0.5-1 Hz range, and scaled by the standard deviation of each trace. Time is relative to the start of the recordings, and is synchronised with the waveforms shown in Fig. 1.

orientation bins. As was also concluded by Wang et al. (2018) from analysing the directional dependence of the signal-to-noise
105 ratio, no directionality of the mean power is observed. Moreover, the variability within a given frequency band exceeds one order of magnitude. Wang et al. (2018) interpreted this as an effect of the heterogeneous site response, which likely exerts a first-order control on the amplitudes and directionality of the ground motions. This will be demonstrated in more detail in Section 3.4.

3.2 Beamforming results of the nodal and DAS arrays

110 To set a baseline, we first beamform the P- and S-waves recorded by the nodal array for each component separately. To visualise the coherence of the wavefield in each direction, we select a 10-second time window starting a few seconds before the P-arrival. The waveforms are then ordered by distance from the earthquake epicentre, band-pass filtered in the 0.5-1 Hz range, and each trace is scaled by its standard deviation – see Fig. 3. In particular the vertical waveforms exhibit very strong coherence across the entire array. Among the horizontal components, the N-component is more coherent, consistent with a source that is oriented almost directly south of the array (with a back-azimuth of 157° from the centre of the array). Similarly, the S-waves (not shown here) exhibit strong coherence particularly in the E-direction, followed by the N- and Z-directions.
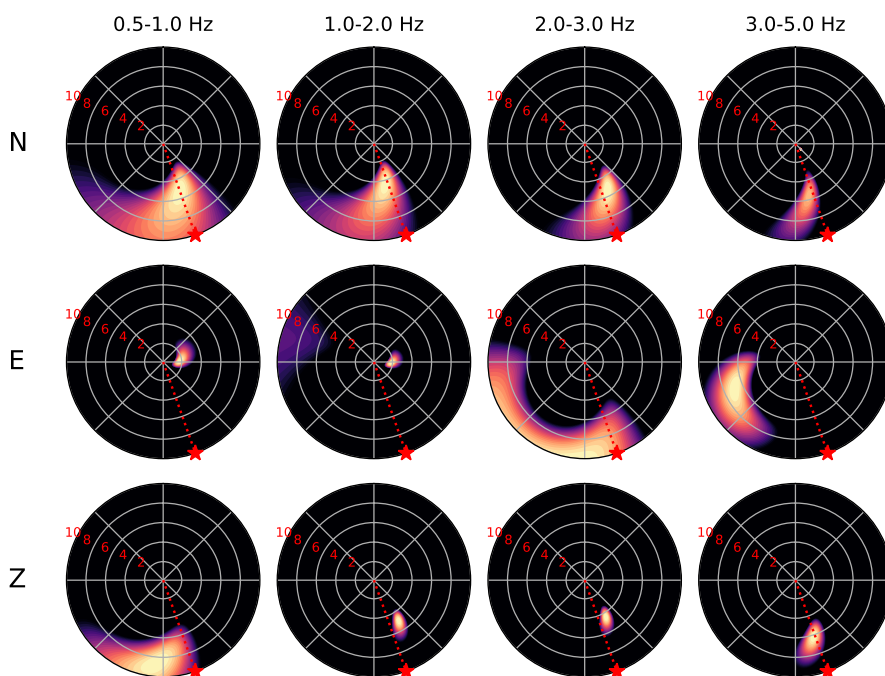
Figure 4. Beamforming results of the P-waves recorded by the nodal array. Each panel shows the MUSIC pseudo-power for the candidate combination of azimuth and apparent velocity (reciprocal of slowness) normalised to lie between 0 and 1. For visual clarity we clip the colours at a normalised pseudo-power of 0.8 (i.e. at 80 % of the maximum pseudo-power). The apparent velocity is plotted up to $10 \ \mathrm{km \, s^{-1}}$, with radial grid increments of $2 \ \mathrm{km \, s^{-1}}$ (indicated by the red numbers). The frequency bands and components are indicated above each column and beside each row, respectively. The true back-azimuth of the source is indicated by a red star in each panel.

The P-wave beamforming results for the nodal array (Fig. 4) show a well-resolved source in the southeast, with an azimuth close to the true back-azimuth of $157°$. As expected from the waveform coherence, this source is most stable and well-resolved for the vertical component, with an apparent propagation velocity between 4 and $6 \ \mathrm{km \, s^{-1}}$. The beams formed from the N-

120   component also indicate a southeast direction-of-arrival, but with a less well-resolved apparent velocity. The beams formed from the E-component suggest weak, poorly resolved sources in the south, west, and east, which are likely scattered P-waves. The sources indicated by beamforming of the S-wave (Fig. 5) are even better resolved than the P-wave sources, particularly in the E-component, with an apparent propagation velocity between 2 and $4 \ \mathrm{km \, s^{-1}}$. For an assumed true P- and S-wave speeds of 2.1 and $1.3 \ \mathrm{km \, s^{-1}}$, respectively (crudely estimated from Feigl and the PoroTomo Team, 2018), the inferred apparent velocities

125   would correspond with an inclination of the direction-of-arrival of $65°$ (consistent with the ratio of vertical to horizontal amplitudes of the nodal P-waveforms).

In strong contrast to the nodal array, the P- and S-waveforms recorded by the DAS array show a low degree of coherence (Fig. 6). While individual cable segments may exhibit some internal coherence (analysed further in Section 3.4), this coherence
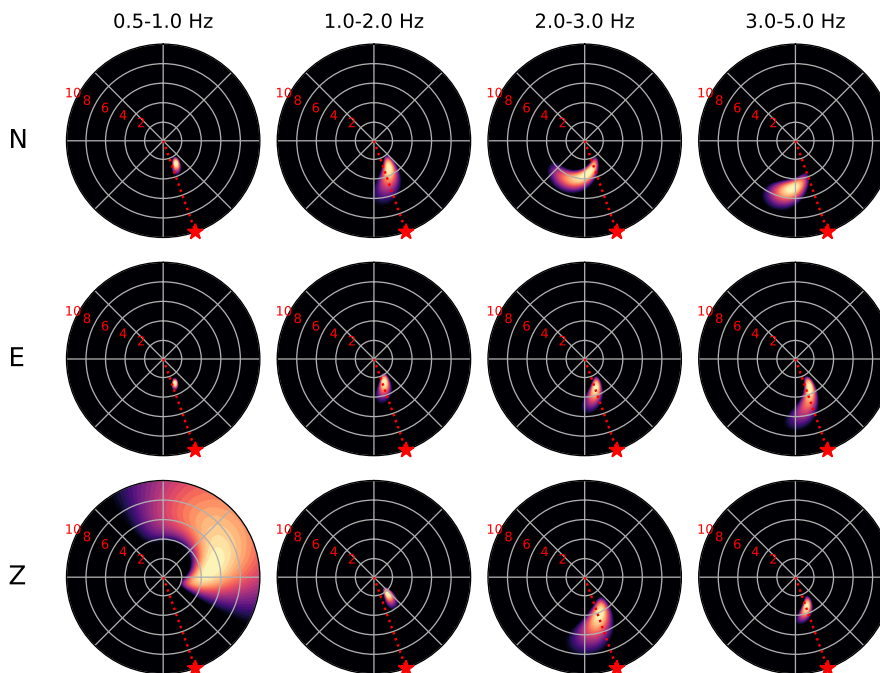
Figure 5. Beamforming results of the S-waves recorded by the nodal array. The panel representation is the same as in Fig. 4.

does not persist across the array. There are several factors that contribute to the incoherence of the recorded signals. Firstly, for
130   a horizontal cable, the DAS strain is a combination of gradients of the two horizontal components of the wavefield, which may
lead to unfavourable interference. Secondly, the amplitudes of the DAS recordings depend strongly on the coupling of the fibre-
optic cable to the ground (Wang et al., 2018) and on the angle of incidence of the incoming plane wave (Martin et al., 2018),
so that various segments at different locations and with different fibre orientations experience variable signal-to-noise ratios.
Thirdly, depending on the orientation of the fibre, polarity flips are anticipated (Fang et al., 2020). Lastly, spatial gradients of
135   the particle velocity (i.e. strain rates) are highly sensitive to local heterogeneities (Singh et al., 2020), and their amplitudes are
inversely proportional to the apparent phase velocity so that slow waves (often scattered waves) are amplified.

When we nonetheless continue to perform beamforming on the DAS array recordings, we obtain highly variable results
(Fig. 7). At the lower frequencies (below 2 Hz), we find a diffuse spread of pseudo-power over a range of potential source
azimuths and apparent velocities. By contrast, at the higher frequencies, we find several well-resolved sources pointing in the
140   southeast and east directions, but with very low apparent velocities (less than $2 \mathrm{~km~s^{-1}}$). These apparent velocities between 1
and $2 \mathrm{~km~s^{-1}}$ are consistent with the inferred S-wave speeds at depths of a few hundred metres, suggesting a shallow "source"
(most likely a seismic scatterer). As mentioned above, slow phase velocities amplify the recorded DAS strain rates, and so
it is not unexpected that, in the absence of strong coherent direct arrivals, slow, scattered waves dominate the beamforming
solutions. Also recall that through the definition of the covariance matrix, the absolute amplitude of the recorded signals
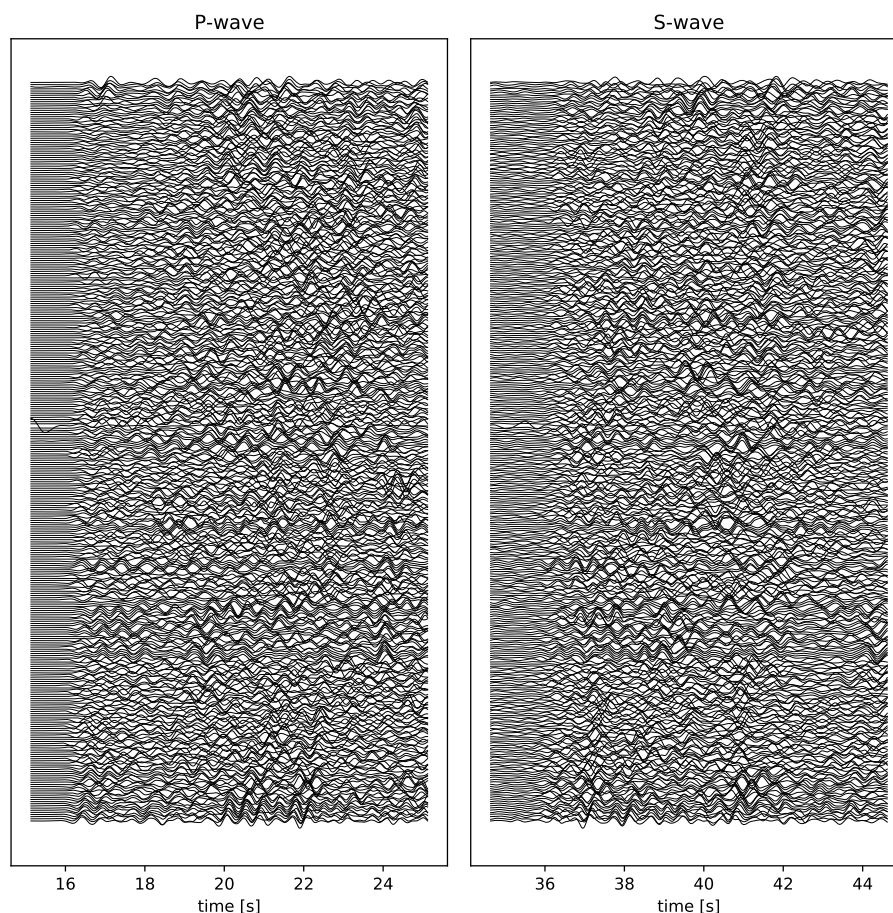
Figure 6. P- and S-waveforms recorded by the DAS array, ordered by distance from the earthquake epicentre, filtered in a 0.5-2 Hz pass band, and scaled by the standard deviation of each trace. Time is relative to the start of the recordings, and is synchronised with the waveforms shown in Fig. 1. For clarity, only every 20th channel waveform is plotted.

145 is irrelevant, which partially addresses the issues of (potential) directionality and ground coupling. However, the wavefield is composed of multiple waves (e.g. direct and scattered arrivals) and their relative phase amplitudes may vary with fibre orientation, which still affects the pseudo-power.

3.3   Simulating DAS recordings from the nodal array

In the previous section, we pointed out several potential reasons for the lack of waveform coherence and the inconsistent

150 beamforming results. In the following section, we will explore one of these factors that is inherent to the DAS measurement principle: the one-dimensional strain rate measurement that aggregates multiple components of the particle velocity field. A
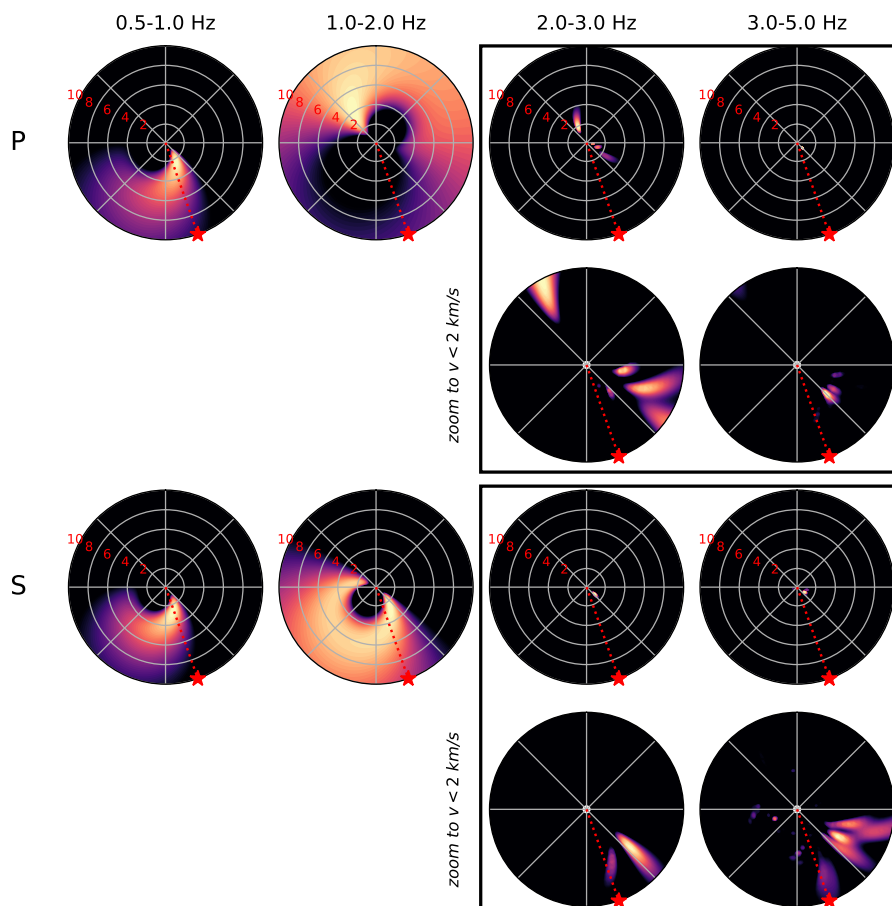
Figure 7. Beamforming results of the P- and S-waves recorded by the DAS array. The panel representation is the same as in Fig. 4. To be able to visually resolve the slow sources at frequencies greater than 2 Hz, we add additional panels magnifying the region up to an apparent velocity of 2 km s^{-1}.

DAS measurement provides only on component of strain, the longitudinal strain along the direction of the fibre. This limitation can be mitigated by making the measurements along helically-wound cables (Kuvshinov, 2016), but since such cable designs were not deployed during the PoroTomo experiment, one has to resort to alternative approaches.

155   As has been clearly demonstrated by Wang et al. (2018), the particle velocity measurements recorded on two nodal seismometers separated by a small distance $2L$ can be accurately converted into the average longitudinal strain rate $\dot{\varepsilon}$ between the two nodes (expressed here at their midpoint x):

$$\dot{\varepsilon}(x) = \frac{1}{2L} \left[\dot{u}(x+L) - \dot{u}(x-L) \right] \tag{3}$$

where $\dot{u}$ is the particle velocity in the direction parallel to the positional difference vector between the two nodes. This average strain rate is equal (or proportional) to the DAS strain measured along a gauge length $2L$ whose end points are co-located with the nodes, if the cable is straight and has a spatially uniform coupling between the two nodes. Given the density of the nodal array, in which most nodes are positioned less than 100 m from its nearest neighbour, we can use this relationship to simulate the response of a DAS array to the strain field induced by the Hawthorne earthquake, and test the effect of superimposing multiple independent components on the beamforming performance. To this end, we triangulate the node coordinates (Fig. 8a), yielding pairs of stations that define each edge in the mesh. For node pairs separated by a distance less than 80 m, we rotate the horizontal (N and E) components of velocity onto the 'virtual' DAS fibre orientation θ as $\dot{u} = \dot{u}^{\mathrm{N}} \sin\theta + \dot{u}^{\mathrm{E}} \cos\theta$. Substitution of $\dot{u}$ into Eq. (3) yields the strain rate along the simulated DAS fibre at the midpoint between each pair of stations (414 in total):

$$\dot{\varepsilon}\left(\frac{x_A + x_B}{2}, \frac{y_A + y_B}{2}\right) = \frac{\left(\dot{u}_A^{\mathrm{N}} - \dot{u}_B^{\mathrm{N}}\right)\sin\theta + \left(\dot{u}_A^{\mathrm{E}} - \dot{u}_B^{\mathrm{E}}\right)\cos\theta}{\sqrt{\left(x_A - x_B\right)^2 + \left(y_A - y_B\right)^2}} \tag{4}$$

where the subscripts A and B indicate the two seismometers between which the strain rate is calculated, each located at a coordinate point (x, y).

The resulting simulated strain rate P-waveforms are shown in Fig. 8b, for selected segments with an orientation within $\pm 10°$ from the event back-azimuth (red segments in Fig. 8a). Even though individually the N- and E-components recorded by the nodal stations exhibit some coherence across the array (see Fig. 3), the horizontal strain rates, involving differences of velocities on two horizontal components, are not coherent. Moreover, if the strain rate (the gradient of the particle velocity field) is calculated only on the basis of the strongly coherent N- or Z-components (Fig. 8c and d, respectively), then the coherence that is seen in the particle velocity measurements (Fig. 3) is almost completely lost. This indicates that it is not just the superposition of two components that causes destructive interference, but that this is caused by the gradient operator itself (regardless whether this operation be done mathematically, like was done here, or physically, like in a DAS fibre). Also, since only segments were selected that are near-parallel to each other, the lack of waveform coherence cannot be attributed to directionality effects.

When we perform the beamforming on the P-waveforms recorded by the virtual DAS array (all segments; Fig. 9), the only sources that stand out are those with very slow apparent phase velocity ($< 2\,\mathrm{km\,s^{-1}}$) and azimuths that vary from west to east. Since the overall waveform coherence across the array is low, these sources likely result from subregions in the array that locally exhibit moderate coherence, but which does not persist throughout the array. Owing to the directional sensitivity of the (simulated) DAS measurement, combining segments of different orientations may affect the beamforming results. We repeated the beamforming on selected segments with an orientation $\pm 10°$ from the event back-azimuth (see Fig. 8a). When only these sub-parallel segments are selected, an ambiguous source arises in the west with high apparent velocity, which is inconsistent with the back-azimuth and apparent phase velocities of the seismic source. This exercise demonstrates that the measurement principle of DAS challenges beamforming methods that are traditionally applied to particle velocities rather than to strain rates. Since we derived the strain rates directly from the nodal seismometers, the lack of coherence and beam resolution seen in the
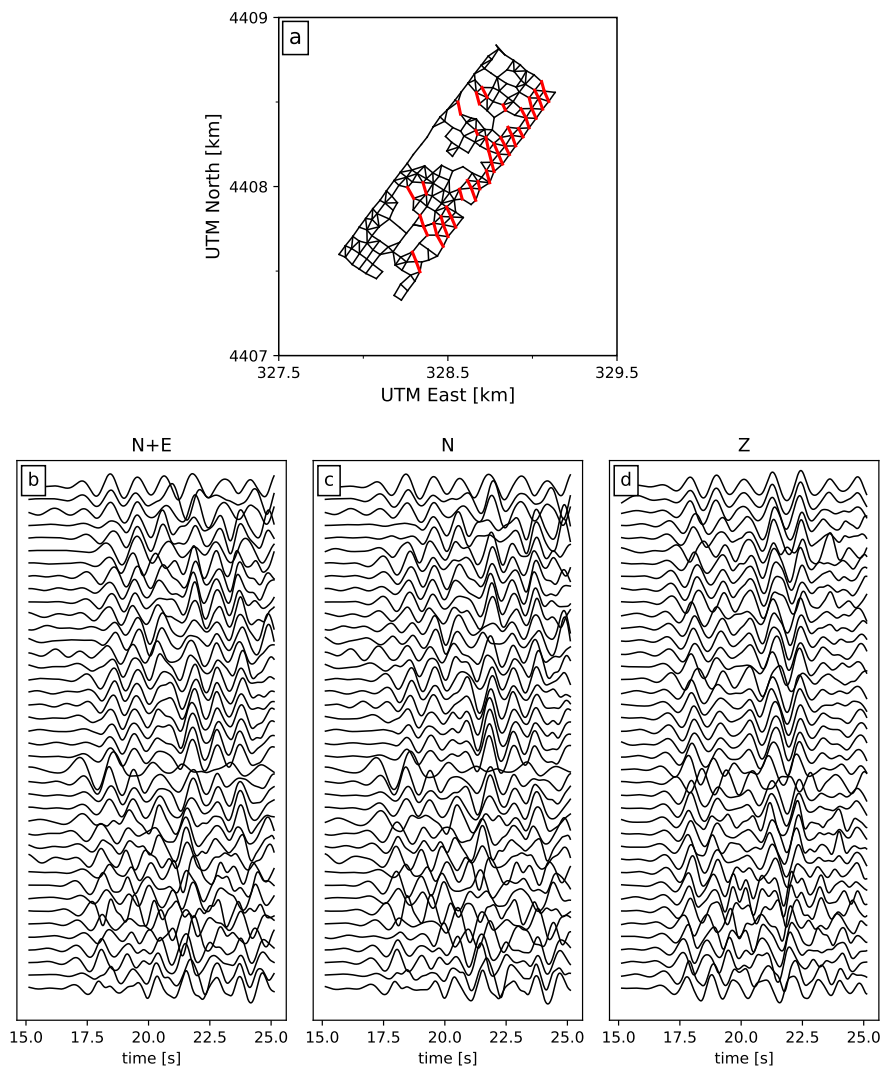
Figure 8. a) Layout of the virtual DAS array, defined by the edges connecting two nodal seismometers separated by less than $80\,\mathrm{m}$ in distance; b-d) P-waveforms recorded by the virtual DAS array for segments with an orientation $\pm 10°$ with respect to the back-azimuth of the seismic source (indicated in red in a)), ordered by distance from the seismic source, filtered in a 0.5-1 Hz pass band, and scaled by the standard deviation of each trace. In b), the waveforms are a superposition of the N- and E-components of the nodal seismometers, while in c) and d) only the N- and Z-components are used, respectively.

DAS data (Figs. 6 and 7) cannot be attributed to DAS-specific technicalities like coupling of the DAS cable with the ground or phase unwrapping artefacts, since the nodal seismometers and their derived data do not suffer from this.
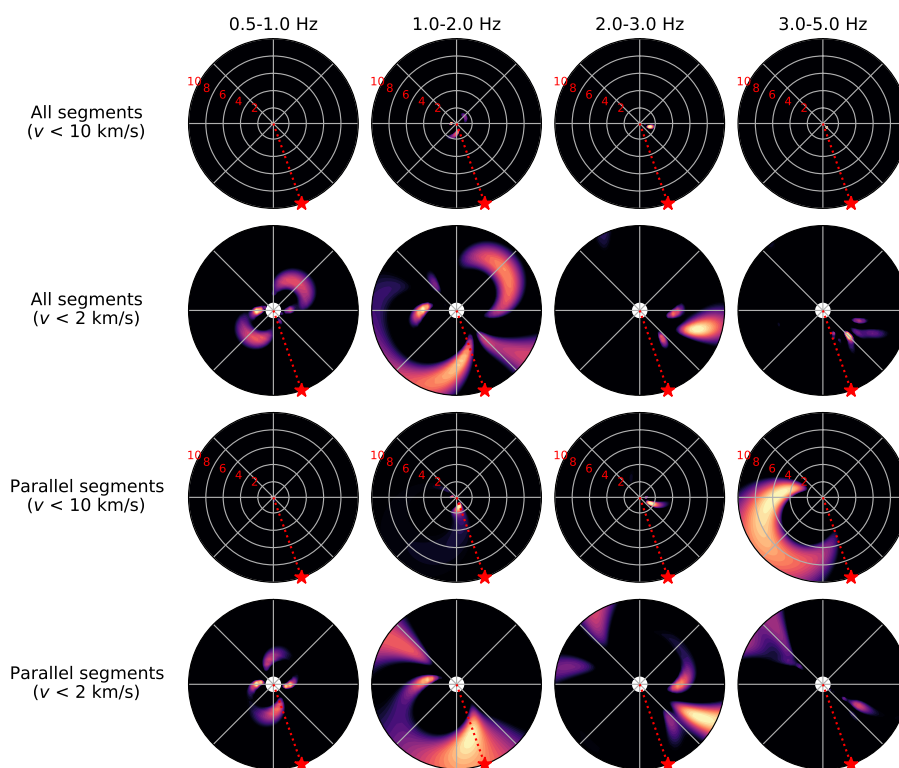
Figure 9. Beamforming results of the P-waveforms recorded by the virtual DAS array, derived from the E- and N-components of the nodal seismometers (i.e. Eq. (4)). The panel representation is the same as in Fig. 4. Each second row of panels is a magnification of the upper row, highlighting the sources with low apparent phase velocity ($< 2 \, \mathrm{km \, s^{-1}}$). The upper two rows are the results of beamforming all the segments, while the lower rows are the results of beamforming only sub-parallel segments (indicated in red in Fig. 8a).

3.4 Selective beamforming of the DAS array

195 Even though the DAS array as a whole does not exhibit strong waveform coherence, there are short individual segments that do exhibit excellent coherence locally. Examples of this can be found in Wang et al. (2018) (their Fig. 14), who selected three segments to estimate the apparent P-wave speed from the first P-wave arrivals recorded by the DAS fibre. The apparent phase velocities obtained from this analysis ranged from 1.124 to $1.452 \, \mathrm{km \, s^{-1}}$, which are much lower than the apparent velocities obtained from the nodal array beamforming (between 4 and 6 $\mathrm{km \, s^{-1}}$), and are suggestive of a shallow, scattered source.

200 Since these segments exhibit strong waveform coherence (Fig. 10), we can attempt to form a stable beam by selecting only the channels associated with these segments.
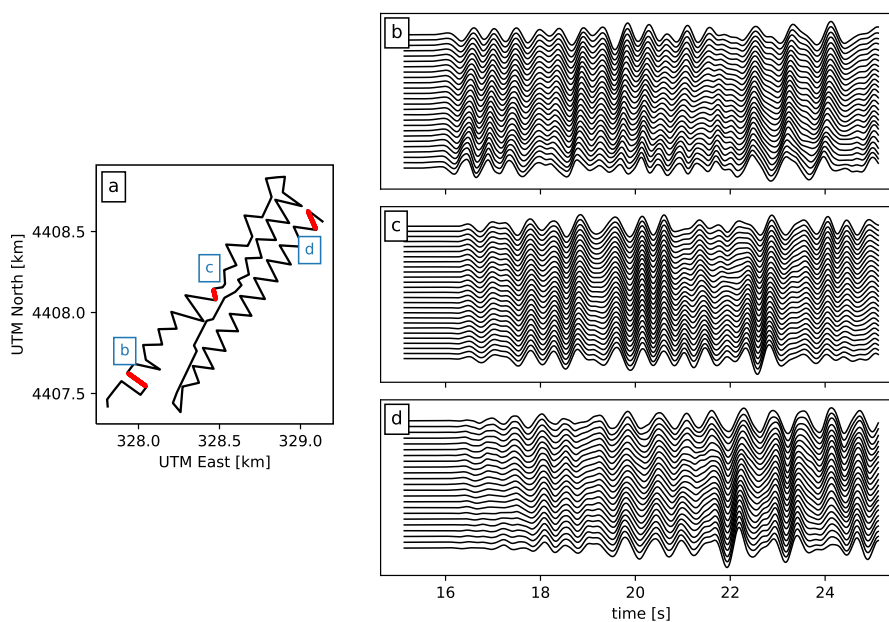
Figure 10. Location of the selected DAS cable segments, indicated in red in panel a. The corresponding P-waveforms that are shown in panels b, c, and d are filtered in a 0.5-2 Hz pass band and scaled by the standard deviation of each trace.

Beamforming on multiple small, linear segments comes with additional challenges. First of all, even though the waveforms may be coherent within one segment, they are not necessarily coherent between segments, which affects the beamforming performance when the waveforms of all the segments are combined. On the other hand, if beamforming is performed on each

205   segment individually, ambiguity arises from the linear geometry of the segments. A plane wave travelling parallel to the length of the cable at a high speed will induce the same phase shift as a plane wave impinging on the cable with a larger angle but at a lower speed. In other words, there exists a perfect trade-off between back-azimuth and apparent velocity for linear segments. This trade-off is most clearly seen when plotting the beam pseudo-power in a space spanned by the azimuth and apparent slowness (reciprocal apparent velocity), in which the beam pseudo-power will appear as a straight line perpendicular to the

210   orientation of the cable (see Fig. 11; see also Fig. 2e in Lindsey et al. (2019)). This ambiguity can be resolved by combining the beamforming results of multiple segments: the source azimuth and slowness that produces the phase shifts consistent with all segments is the one where the linear bands of beam power intersect. As laid out by Rieken and Fuhrmann (2004), the intersection of the invididual signal spaces of all subarrays can be found by the method of projection onto convex sets. From this analysis, it follows that the signal space of M subarrays combined furnish a block matrix, which upon substitution into the
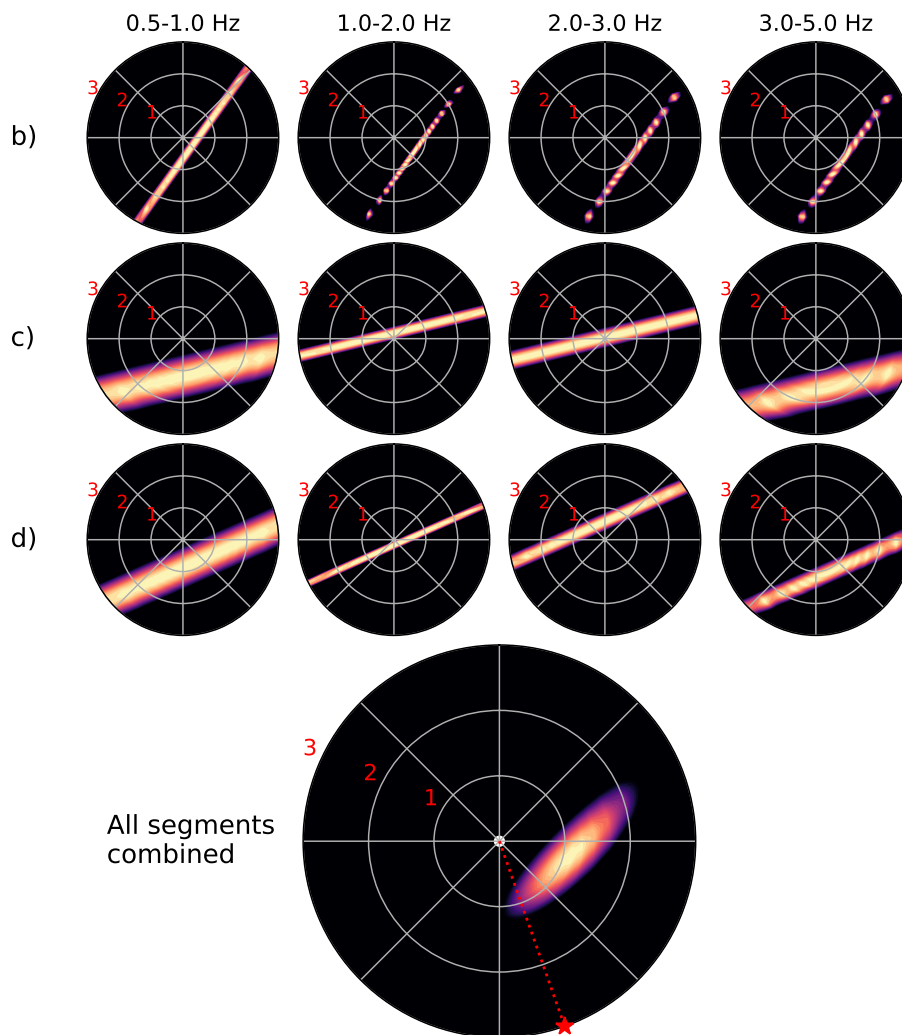
Figure 11. Beamforming results of the P-waveforms recorded on selected segments of the DAS array. In this figure, the panels show pseudo-power $\hat{P}$ normalised by the maximum power, such that $0 \leq \hat{P} \leq 1$, plotted as a function of the back-azimuth and apparent slowness of the candidate source. The slowness values (in $\mathrm{s\,km^{-1}}$) of the radial grid lines are as indicated by the red numbers. The letters indicated on the left of each row correspond to the panels in Fig. 10.

215 definition of the MUSIC spectrum yields (Rieken and Fuhrmann, 2004):

$$\hat{P} = \left(\sum_{m=1}^{M} \mathbf{a}_m^H \mathbf{G}_m \mathbf{G}_m^H \mathbf{a}_m \right)^{-1} = \left(\sum_{m=1}^{M} \hat{P}_m^{-1} \right)^{-1} \tag{5}$$

with $\mathbf{G}_m$ representing the projection onto the noise-subspace of the covariance matrix $\mathbf{C}_m^2$ (as defined in Eq. (2)) and $\mathbf{a}_m$ the steering vector of the m-th subarray, and the superscript H denoting the conjugate transpose. In other words, the analysis of the intersections of signal subspaces of the subarrays naturally leads to a harmonic mean of the MUSIC pseudo-spectra of each

220   subarray. When applying this rationale to the subarray beams presented in Fig. 11, we obtain a combined beam which shows a well-resolved source with a back-azimuth towards the east and an apparent slowness of $1.2\ \mathrm{s\,km^{-1}}$ ($0.83\ \mathrm{km\,s^{-1}}$). Consistent with our previous interpretations, the azimuth and phase velocity of this source are incompatible with direct P-wave arrivals from the Hawthorne earthquake; it is therefore interpreted as a shallow scattered wave.

  Since the internal waveform coherence of each segment varies across the array (and also with the selected frequency band),
225   manually selecting a few segments for the beamforming may introduce a bias. However, if internal waveform coherence is the main selection criterion, whether or not to include individual segments in the beamforming analysis can be determined on the basis of the L_2-norm of the covariance matrix, i.e.:

$$c^2 = \frac{1}{N^2} \sum_i \sum_j C_{ij} \bar{C}_{ij} \tag{6}$$

where N is the number of channels in a given segment for which the covariance matrix C_{ij} is computed. We compute c^2 for the
230   P-waveforms of each quasi-linear segment of the cable over the 0.5-1 Hz frequency band, and select those segments with $c^2 >$ 0.9 (six in total; Fig. 12a). Since these segments are all linear, we obtain ambiguous results in terms of the azimuth and apparent velocity (which trade-off with one another), but within this ambiguity the sources are well resolved (Fig. 12b). However, while most of the selected segments suggest a direction-of-arrival between the east and the south with a maximum apparent velocity of 2-3 $\mathrm{km\,s^{-1}}$, there are two segments that suggest a direction-of-arrival from the north with a maximum apparent velocity at
235   around 1 $\mathrm{km\,s^{-1}}$, which most likely signify the predominance of locally scattered waves. When we combine the beam pseudo-power of each segment through Eq. (5), we obtain an apparent source with a back-azimuth pointing northeast, and an apparent velocity of 0.7 $\mathrm{km\,s^{-1}}$ (Fig. 12c). At first, this seems counter-intuitive, as none of the segments seem to suggest a source northeast of the array, while the combined result does. Moreover, the combined apparent velocity is substantially less than the maximum apparent velocities of all the segments individually. However, these results are a direct consequence of the harmonic
240   averaging procedure adopted here, which implictly assumes that the wavefields at all selected subarrays are dominated by the same sets of waves: maximising the MUSIC pseudo-spectra at the intersection of the signal spaces of all the segments becomes problematic for sources that are diametrically opposite of each other (e.g. north-south), as the intersection of the signal spaces occurs only at infinity when representing the pseudo-power in slowness space (or at the origin in velocity space). This then leads to the diffuse spread of pseudo-power seen in Fig. 12c with the maximum pseudo-power at high slowness values.

245   When we exclude the two segments with an apparent source north of the array, we obtain a maximum beam power at an azimuth of 122° and apparent velocity of 2.0 $\mathrm{km\,s^{-1}}$. While this result is in better agreement with the true direction of arrival of the seismic source (157° with an apparent P-wave speed of 4-6 $\mathrm{km\,s^{-1}}$, as inferred from the nodal array), the discrepancy is substantial. Particularly the low apparent velocity inferred from the DAS segments is suggestive of the arrival of scattered waves rather than direct waves. Regardless, this result is only obtained after manual quality control and selection of desired
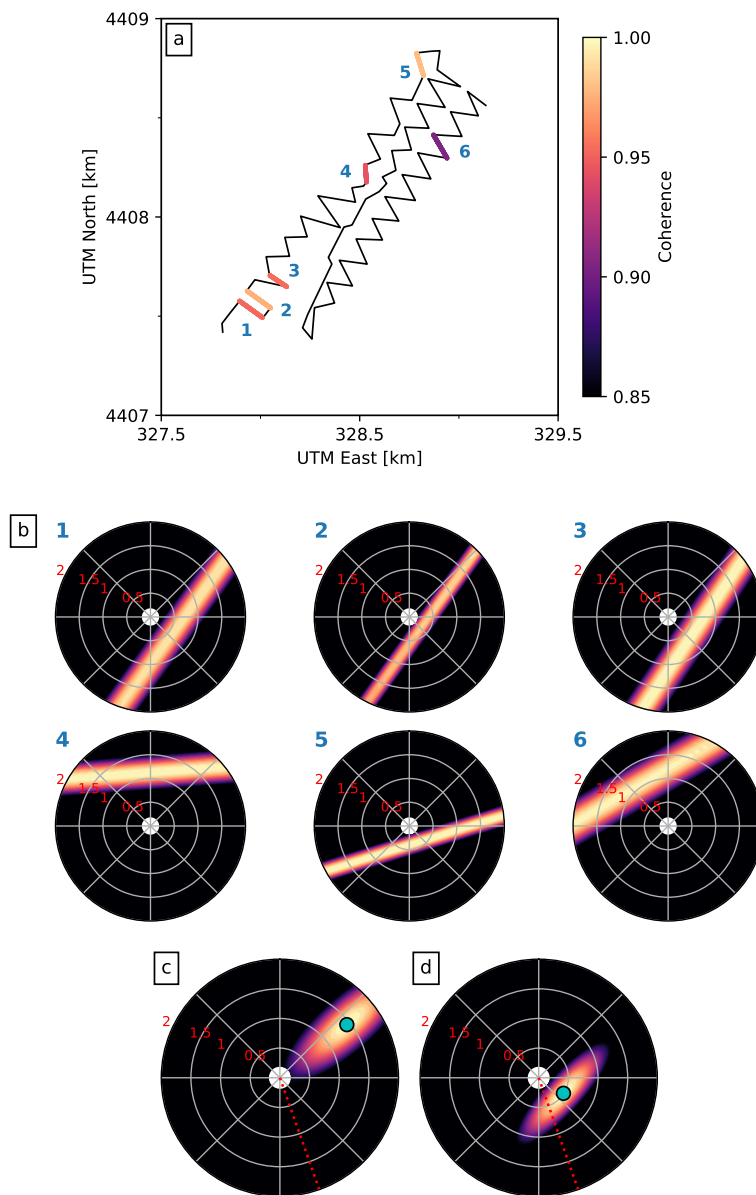
Figure 12. a) Locations and internal coherence of six selected segments along the cable, each indicated by a number; b) Beamforming results in the 0.5-1 Hz frequency band for each of the segments. The slowness values (in $\mathrm{s\,km^{-1}}$) of the radial grid lines are as indicated by the red numbers; c) Beam pseudo-power of all the segments combined through Eq. (5); d) Beam pseudo-power of segments 1, 2, 3, and 5 combined through Eq. (5). In c) and d), the coordinate of the maximum beam power is indicated by a cyan dot.

250   segments. For automated segment selection and beamforming one must be cautious for conflicting directions-of-arrival that lead to artificial results like in Fig. 12c.

4   Discussion

4.1   Importance of site heterogeneities and seismic wave scattering

The purpose of beamforming is to locate the origin of the incoming signals, which requires that the signals be direct arrivals.
255   As the seismic equivalent of acoustic echoes, scattered waves will follow a trajectory different from the direct arrivals, exhibit a different direction-of-arrival, and so appear to originate from a different source location. Throughout this work, we have shown that the DAS array recordings at the Brady Hot Springs natural laboratory are strongly affected by scattered waves and local heterogeneities. However, the nodal seismometer array seems much less affected, and displays strong signatures of the Hawthorne earthquake's direct arrivals. To summarise, the likely reasons for this are as follows:

260   1. For P- and S-waves, DAS strain rate measurements are most sensitive to strains parallel to the direction of the fibre (Martin et al., 2018). Direct arrivals originating from a distant source arrive at the array at a steep inclination, and so their projection onto the direction of a horizontal fibre is comparatively small (for P-waves, the DAS sensitivity exhibits a $\cos^2$ decay with inclination). By contrast, free-surface topography and shallow subsurface heterogeneities may cause scattered seismic waves to arrive at the array at a shallow inclination, so that these are greatly amplified in the DAS
265   measurements.

    2. As pointed out by Daley et al. (2016), the relation between the strain ε induced by a plane wave and the particle velocity $\dot{u}$ in the along-fibre direction is $\varepsilon = \pm\frac{1}{c}\dot{u}$, with c being the apparent phase velocity of the medium. This implies that apparent fast waves (i.e. arriving at steep inclinations) are damped with respect to sub-horizontally-travelling waves such as those generated by shallow scattering.

270   3. From the numerical simulations and theoretical analysis of Singh et al. (2020), it is immediately clear that gradients in the particle velocity field are highly sensitive to heterogeneities. Since the subsurface beneath the Brady Hot Springs site is strongly heterogeneous (Feigl and the PoroTomo Team, 2018), spatial variations in the phase velocity are expected to exert a strong influence on the DAS measurements. The lack of observable directional sensitivity of the DAS array (our Fig. 2 and Fig. 22 of Wang et al. (2018)) further attest to this. Singh et al. (2020) proposed that a correction term
275   (the "coupling tensor") may be inverted for, so that the amplitudes of the recordings may be adjusted to represent the "true" velocity gradients. Since the true particle velocity field is known (being recorded by the nodal array), this offers an interesting perspective for future analysis of the Brady Hot Springs data set.

    4. Lastly, even when considering the directional sensitivity of DAS, the locally recorded strain rates appear to be highly incoherent, while the particle velocity measurements themselves exhibit very strong coherence (compare Fig. 3 with

Fig. 8). The superposition of multiple orthogonal components of the particle velocity field may lead to additional de-
structive interference, even though this was not clearly seen in our analysis in Section 3.3 (see Fig. 8b).

As summarised by Shearer (2015), the effects of phase velocity heterogeneities are most pronounced when the size of the
heterogeneity is similar to the seismic wavelength. Owing to a scarcity of large-scale heterogeneities, low frequency signals
may be less affected by seismic scattering. Coincidentally, the DAS beamforming results in the lowest frequency band (0.5-
1 Hz; Fig. 7) do suggest a source with an azimuth that corresponds with the true back-azimuth, although the spread in the
beam pseudo-power is diffuse. This may be a consequence of the signal-to-noise ratio in the lowest frequency range, since the
source exhibits low spectral power in this range (Fig. 2). Notwithstanding, DAS has a flat frequency response even at very low
frequencies (Lindsey et al., 2020), so that further investigations of DAS beamforming at low frequencies are warranted.

4.2   Implications for beamforming on sparse and dense DAS arrays

The analysis of the PoroTomo experiment has revealed some limitations of conventional beamforming methods applied to DAS
array data, particularly in relation to scattered waves and heterogeneities. However, the Brady Hot Springs geothermal field may
be considered a particularly unfavourable setting for DAS seismic beamforming owing to the complexity of the subsurface.
Fibre-optical cables deployed on more homogeneous bedrock terranes may not suffer as much from high-amplitude shallow
scattering. On the other hand, one of the main promises of DAS is its versatility in deployment conditions, with interesting
deployment targets including "heterogeneous" environments such as urban areas (Dou et al., 2017; Fang et al., 2020) and
submarine basins (Lindsey et al., 2019; Sladen et al., 2019). For many civil monitoring applications, such as traffic density
monitoring (Liu et al., 2018) and vehicle tracking (Wiesmeyr et al., 2020), some of the issues pointed out in the previous
section do not apply, as the signals of interest arrive at the DAS fibre at a shallow (or zero) inclination. However, for the
purpose of localising deep or distant sources, the inclination sensitivity of DAS starts to become directly relevant.

A second unfavourable aspect of the PoroTomo dataset is that the DAS array is deployed within a relatively small region
(1500 by 500 m), which limits the resolution of beamforming methods (being proportional to the span of the array). Sparse
L-shaped and quasi-linear array configurations provide a much larger array span, at the expense of increased source azimuth
ambiguity inherent to linear arrays. As was done in Section 3.4, multiple segments of variable orientations can be combined
to resolve this ambiguity. Moreover, the same procedure can be adopted to extract the signals carried by direct arrivals: in
the case of the Brady Hot Springs geothermal site, the entire array receives seismic energy from (potentially) multiple nearby
scattering sites, obscuring the direct arrivals. By contrast, sparse arrays that extend over long distances may receive seismic
energy from different scattering sites along the trace of the cable. By selecting and combining the beam power of several
segments following the harmonic averaging method proposed by Rieken and Fuhrmann (2004), sources that are common to
all segments are amplified with respect to segment-specific sources (i.e. scatterers), provided that the direct arrivals exhibit a
sufficiently large footprint in all segments. Large sparse arrays may therefore be more suitable for seismic beamforming than
compact dense arrays.

One key assumption that underlies beamforming is that the signal is carried by a plane wave. This assumption implicitly requires that the source be distant compared to the extent of the array. Moreover, the phase velocity is assumed to be uniform across the array. Both these assumptions are embedded in the definition of the steering vectors through the time delay τ (see

315 Eq. (1)). Since DAS on fibre-optic cables of several tens of kilometres in length has been demonstrated to be feasible (Lindsey et al., 2019; Sladen et al., 2019), these assumptions may break down for local and regional seismic sources. Moreover, for e.g. earthquake early warning purposes, fault zones may be instrumented with fibre-optic cables running along-strike for many tens of kilometres, so that the finite extent of the rupture and rupture complexity will prevent the application of beamforming methods. Fortunately, the plane wave and uniform velocity assumptions can be relaxed by directly computing the travel time

320 between a candidate source location and a location along the cable, turning the beamforming problem into a back-projection exercise (Kiser and Ishii, 2017). Alternatively, the azimuth estimates derived from beamforming on individual segments can be combined to produce a triangulated source location (e.g. Hutchison and Ghosh, 2017; Stipčević et al., 2017). In both cases, the source localisation results will greatly benefit from the large lateral extent of the DAS arrays.

5   Conclusions

325 This study considered the potential of fibre-optic Distributed Acoustic Sensing (DAS) arrays for the purpose of seismic beamforming. This was done by performing beamforming on the ground motions generated by the March 2016 M_L 4.3 Hawthorne earthquake, as recorded by a DAS array co-located with a dense nodal seismometer array at the Brady Hot Springs geothermal field. Comparing the waveforms recorded by DAS with those recorded by the nodal seismometers, we find that the strong waveform coherence of the nodal array is absent in the DAS array. Since the quality of the beamforming results depends

330 strongly on waveform coherence, the DAS array is unable to produce a robust source azimuth and apparent velocity, whereas the nodal array produces an extremely well-resolved source location that is consistent with the true back-azimuth of the earthquake epicentre. Instead, beamforming on the DAS array reveals source locations that likely correspond with shallow seismic scattering sites. We attribute the lack of DAS waveform coherence to the DAS measurement principle, which inherently leads to diminished sensitivity of DAS recordings to the direct arrivals, supposedly arriving at the array at a steep inclination, and

335 amplifies scattered waves arriving at shallow inclinations. Moreover, we demonstrate that the spatial gradients of the particle velocity field (i.e. strain rate) exhibit far lower coherence than do the particle velocity waveforms, which additionally impedes beamforming. Compared to other DAS arrays, this may be aggravated by the strong phase velocity heterogeneities present at the Brady Hot Springs geothermal field. Nonetheless, many of these issues may be resolved by expanding the extent of the array, and through the combination of the beamforming results of individual segments along the fibre-optic cable.

340 *Code and data availability.* Python scripts that reproduces the results and figures in this manuscript are available at https://doi.org/10.6084/m9.figshare.12899288.

Author contributions. MvdE conceptualised the study and performed the analyses. JPA supervised MvdE and contributed to methodology and interpretation. Both authors discussed and prepared the contents of the manuscript.

Competing interests. The authors declare no competing interests

345   *Acknowledgements.* This work was supported by the French government through the UCA^{JEDI} Investments in the Future project managed by the National Research Agency (ANR) with the reference number ANR-15-IDEX-01. The authors thank Lingsen Meng for sharing his MUSIC back-projection codes, from which the beamforming codes used in this study were derived. The nodal seismometer data were processed using ObsPy (Beyreuther et al., 2010). Data visualisation was done using Matplotlib (Hunter, 2007).

References

350 Ajo-Franklin, J., Dou, S., Daley, T., Freifeld, B., Robertson, M., Ulrich, C., Wood, T., Eckblaw, I., Lindsey, N., Martin, E., and Wagner, A.: Time-Lapse Surface Wave Monitoring of Permafrost Thaw Using Distributed Acoustic Sensing and a Permanent Automated Seismic Source, in: 2017 SEG International Exposition and Annual Meeting, Society of Exploration Geophysicists, 2017.

Beyreuther, M., Barsch, R., Krischer, L., Megies, T., Behr, Y., and Wassermann, J.: ObsPy: A Python Toolbox for Seismology, Seismological Research Letters, 81, 530–533, https://doi.org/10.1785/gssrl.81.3.530, 2010.

355 Capon, J., Greenfield, R., and Kolker, R.: Multidimensional Maximum-Likelihood Processing of a Large Aperture Seismic Array, Proceedings of the IEEE, 55, 192–211, https://doi.org/10.1109/PROC.1967.5439, 1967.

Cole, S., Karrenbach, M., Kahn, D., Rich, J., Silver, K., and Langton, D.: Source Parameter Estimation from DAS Microseismic Data, in: 2018 SEG International Exposition and Annual Meeting, Society of Exploration Geophysicists, 2018.

Daley, T. M., Miller, D. E., Dodds, K., Cook, P., and Freifeld, B. M.: Field Testing of Modular Borehole Monitoring with Simultaneous 360 Distributed Acoustic Sensing and Geophone Vertical Seismic Profiles at Citronelle, Alabama, Geophysical Prospecting, 64, 1318–1334, https://doi.org/10.1111/1365-2478.12324, 2016.

Dou, S., Lindsey, N., Wagner, A. M., Daley, T. M., Freifeld, B., Robertson, M., Peterson, J., Ulrich, C., Martin, E. R., and Ajo-Franklin, J. B.: Distributed Acoustic Sensing for Seismic Monitoring of The Near Surface: A Traffic-Noise Interferometry Case Study, Scientific Reports, 7, 11 620, https://doi.org/10.1038/s41598-017-11986-4, 2017.

365 Fang, G., Li, Y. E., Zhao, Y., and Martin, E. R.: Urban Near-Surface Seismic Monitoring Using Distributed Acoustic Sensing, Geophysical Research Letters, 47, e2019GL086 115, https://doi.org/10.1029/2019GL086115, 2020.

Feigl, K.: Brady's Geothermal Field DAS Earthquake Data, https://doi.org/10.15121/1334285, 2016a.

Feigl, K.: Brady's Geothermal Field Nodal Seismometer Earthquake Data, https://doi.org/10.15121/1334284, 2016b.

Feigl, K. L. and the PoroTomo Team: Overview and Preliminary Results from the PoroTomo Project at Brady Hot Springs, Nevada: Poroe-370 lastic Tomography by Adjoint Inverse Modeling of Data from Seismology, Geodesy, and Hydrology, in: 43rd Workshop on Geothermal Reservoir Engineering, Stanford University, Stanford, USA, 2018.

Goldstein, P. and Archuleta, R. J.: Array Analysis of Seismic Signals, Geophysical Research Letters, 14, 13–16, https://doi.org/10.1029/GL014i001p00013, 1987.

Hartog, A. H.: An Introduction to Distributed Optical Fibre Sensors, CRC Press, https://doi.org/10.1201/9781315119014, 2017.

375 Hunter, J. D.: Matplotlib: A 2D Graphics Environment, Computing in Science & Engineering, 9, 90–95, https://doi.org/10.1109/MCSE.2007.55, 2007.

Hutchison, A. A. and Ghosh, A.: Ambient Tectonic Tremor in the San Jacinto Fault, near the Anza Gap, Detected by Multiple Mini Seismic ArraysAmbient Tectonic Tremor in the San Jacinto Fault, near the Anza Gap, Detected by Multiple Mini Seismic Arrays, Bulletin of the Seismological Society of America, 107, 1985–1993, https://doi.org/10.1785/0120160385, 2017.

380 Inbal, A., Ampuero, J. P., and Clayton, R. W.: Localized Seismic Deformation in the Upper Mantle Revealed by Dense Seismic Arrays, Science, 354, 88–92, https://doi.org/10.1126/science.aaf1370, 2016.

Inza, L. A., Mars, J. I., Métaxian, J. P., O'Brien, G. S., and Macedo, O.: Seismo-Volcano Source Localization with Triaxial Broad-Band Seismic Array, Geophysical Journal International, 187, 371–384, https://doi.org/10.1111/j.1365-246X.2011.05148.x, 2011.

Jiang, C., Schmandt, B., Ward, K. M., Lin, F.-C., and Worthington, L. L.: Upper Mantle Seismic Structure of Alaska From Rayleigh and S 385 Wave Tomography, Geophysical Research Letters, 45, 10,350–10,359, https://doi.org/10.1029/2018GL079406, 2018.

Jolie, E., Moeck, I., and Faulds, J. E.: Quantitative Structural–Geological Exploration of Fault-Controlled Geothermal Systems—A Case Study from the Basin-and-Range Province, Nevada (USA), Geothermics, 54, 54–67, https://doi.org/10.1016/j.geothermics.2014.10.003, 2015.

Kiser, E. and Ishii, M.: Back-Projection Imaging of Earthquakes, Annual Review of Earth and Planetary Sciences, 45, 271–299,
390   https://doi.org/10.1146/annurev-earth-063016-015801, 2017.

Krüger, F., Weber, M., Scherbaum, F., and Schlittenhardt, J.: Double Beam Analysis of Anomalies in the Core-Mantle Boundary Region, Geophysical Research Letters, 20, 1475–1478, https://doi.org/10.1029/93GL01311, 1993.

Kuvshinov, B. N.: Interaction of Helically Wound Fibre-Optic Cables with Plane Seismic Waves, Geophysical Prospecting, 64, 671–688, https://doi.org/10.1111/1365-2478.12303, 2016.

395 Lellouch, A., Yuan, S., Spica, Z., Biondi, B., and Ellsworth, W. L.: Seismic Velocity Estimation Using Passive Downhole Distributed Acoustic Sensing Records: Examples From the San Andreas Fault Observatory at Depth, Journal of Geophysical Research: Solid Earth, 124, 6931–6948, https://doi.org/10.1029/2019JB017533, 2019.

Lin, F.-C., Li, D., Clayton, R. W., and Hollis, D.: High-Resolution 3D Shallow Crustal Structure in Long Beach, California: Application of Ambient Noise Tomography on a Dense Seismic Array, GEOPHYSICS, 78, Q45–Q56, https://doi.org/10.1190/geo2012-0453.1, 2013.

400 Lindsey, N. J., Dawe, T. C., and Ajo-Franklin, J. B.: Illuminating Seafloor Faults and Ocean Dynamics with Dark Fiber Distributed Acoustic Sensing, Science, 366, 1103–1107, https://doi.org/10.1126/science.aay5881, 2019.

Lindsey, N. J., Rademacher, H., and Ajo-Franklin, J. B.: On the Broadband Instrument Response of Fiber-Optic DAS Arrays, Journal of Geophysical Research: Solid Earth, 125, e2019JB018 145, https://doi.org/10.1029/2019JB018145, 2020.

Liu, H., Ma, J., Yan, W., Liu, W., Zhang, X., and Li, C.: Traffic Flow Detection Using Distributed Fiber Optic Acoustic Sensing, IEEE
405   Access, 6, 68 968–68 980, https://doi.org/10.1109/ACCESS.2018.2868418, 2018.

Martin, E. R., Lindsey, N., Ajo-Franklin, J., and Biondi, B.: Introduction to Interferometry of Fiber Optic Strain Measurements, https://doi.org/10.31223/osf.io/s2tjd, 2018.

Meng, L., Inbal, A., and Ampuero, J.-P.: A Window into the Complexity of the Dynamic Rupture of the 2011 Mw 9 Tohoku-Oki Earthquake, Geophysical Research Letters, https://doi.org/10.1029/2011GL048118, 2011.

410 Meng, L., Allen, R. M., and Ampuero, J.-P.: Application of Seismic Array Processing to Earthquake Early WarningApplication of Seismic Array Processing to Earthquake Early Warning, Bulletin of the Seismological Society of America, 104, 2553–2561, https://doi.org/10.1785/0120130277, 2014.

Nakamichi, H., Yamanaka, Y., Terakawa, T., Horikawa, S., Okuda, T., and Yamazaki, F.: Continuous Long-Term Array Analysis of Seismic Records Observed during the 2011 Shinmoedake Eruption Activity of Kirishima Volcano, Southwest Japan, Earth, Planets and Space, 65,
415   7, https://doi.org/10.5047/eps.2013.03.002, 2013.

Rieken, D. and Fuhrmann, D.: Generalizing MUSIC and MVDR for Multiple Noncoherent Arrays, IEEE Transactions on Signal Processing, 52, 2396–2406, https://doi.org/10.1109/TSP.2004.832153, 2004.

Ringdal, F. and Husebye, E. S.: Application of Arrays in the Detection, Location, and Identification of Seismic Events, Bulletin of the Seismological Society of America, 72, S201–S224, 1982.

420 Schmidt, R.: Multiple Emitter Location and Signal Parameter Estimation, IEEE Transactions on Antennas and Propagation, 34, 276–280, https://doi.org/10.1109/TAP.1986.1143830, 1986.

Shearer, P. M.: Deep Earth Structure: Seismic Scattering in the Deep Earth, in: Treatise on Geophysics (Second Edition), edited by Schubert, G., pp. 759–787, Elsevier, Oxford, https://doi.org/10.1016/B978-0-444-53802-4.00018-X, 2015.

Singh, S., Capdeville, Y., and Igel, H.: Correcting Wavefield Gradients for the Effects of Local Small-Scale Heterogeneities, Geophysical
    Journal International, 220, 996–1011, https://doi.org/10.1093/gji/ggz479, 2020.

425

Sladen, A., Rivet, D., Ampuero, J. P., De Barros, L., Hello, Y., Calbris, G., and Lamare, P.: Distributed Sensing of Earthquakes and Ocean-
    Solid Earth Interactions on Seafloor Telecom Cables, Nature Communications, 10, 1–8, https://doi.org/10.1038/s41467-019-13793-z,
    2019.

Stipčević, J., Kennett, B. L. N., and Tkalčić, H.: Simultaneous Use of Multiple Seismic Arrays, Geophysical Journal International, 209,
    770–783, https://doi.org/10.1093/gji/ggx027, 2017.

430

Thomson, D.: Spectrum Estimation and Harmonic Analysis, Proceedings of the IEEE, 70, 1055–1096,
    https://doi.org/10.1109/PROC.1982.12433, 1982.

Walter, F., Gräff, D., Lindner, F., Paitz, P., Köpfli, M., Chmiel, M., and Fichtner, A.: Distributed Acoustic Sensing of Microseismic Sources
    and Wave Propagation in Glaciated Terrain, Nature Communications, 11, 2436, https://doi.org/10.1038/s41467-020-15824-6, 2020.

435

Wang, H. F., Zeng, X., Miller, D. E., Fratta, D., Feigl, K. L., Thurber, C. H., and Mellors, R. J.: Ground Motion Response to an ML 4.3
    Earthquake Using Co-Located Distributed Acoustic Sensing and Seismometer Arrays, Geophysical Journal International, 213, 2020–2036,
    https://doi.org/10.1093/gji/ggy102, 2018.

Wiesmeyr, C., Litzenberger, M., Waser, M., Papp, A., Garn, H., Neunteufel, G., and Döller, H.: Real-Time Train Tracking from Distributed
    Acoustic Sensing Data, Applied Sciences, 10, 448, https://doi.org/10.3390/app10020448, 2020.

440

Zhan, Z.: Distributed Acoustic Sensing Turns Fiber-Optic Cables into Sensitive Seismic Antennas, Seismological Research Letters, 91, 1–15,
    https://doi.org/10.1785/0220190112, 2020.

Zigone, D., Ben-Zion, Y., Lehujeur, M., Campillo, M., Hillers, G., and Vernon, F. L.: Imaging Subsurface Structures in the San Jac-
    into Fault Zone with High-Frequency Noise Recorded by Dense Linear Arrays, Geophysical Journal International, 217, 879–893,
    https://doi.org/10.1093/gji/ggz069, 2019.